CitcomSVE-3.0: A Three-dimensional Finite Element Software Package for Modeling Load-induced Deformation and Glacial Isostatic Adjustment for an Earth with Viscoelastic and Compressible Mantle

Tao Yuan[1], Shijie Zhong[1], Geruo A[2]

[1]Department of Physics, University of Colorado, Boulder, Colorado, USA

[2]Department of Earth Sciences, University of California at Irvine, California, USA

E-mail: tao.yuan@colorado.edu

Submitted to Geoscientific Model Development

Abstract. Earth and other terrestrial and icy planetary bodies deform visco-elastically under various forces. Numerical modeling plays a critical role in understanding the nature of various dynamic deformation processes. This article introduces a newly developed, open-source package, CitcomSVE-3.0, which efficiently solves the visco-elastic deformation of planetary bodies. Based on its predecessor, CitcomSVE-2.1, CitcomSVE-3.0 is updated to account for 3-D elastic compressibility and depth-dependent density, which are particularly important in modeling horizontal displacement for visco-elastic deformation. We benchmark CitcomSVE-3.0 against a semi-analytical code for two types of loading problems: 1) single harmonic loads on the surface or as tidal force and 2) the glacial isostatic adjustment (GIA) problem with a realistic ice sheet loading history (ICE-6G_D) and an updated version of sea level equations. The benchmark results presented here demonstrate the accuracy and efficiency of this package. CitcomSVE shows a second-order accuracy in terms of spatial resolution. For a typical GIA modeling with 122-ky glaciation-deglaciation history, surface horizontal resolution of ~50 km, and time increment of 125 yr, it takes ~ 3 hours on 384 CPU cores to complete with less than 5% errors in displacement rates.

1. Introduction

Observations and interpretations of solid Earth's displacement and deformation in response to surface loadings and tidal forcing are essential in geoscience for at least three important reasons. First, deglaciation on continents and sea level rise as surface loading processes cause uplifts in glaciated continental regions and subsidence of sea floor, respectively. The amount of sea level rise during the deglaciation process critically depends on solid-Earth's response to such surface loading processes (Mitrovica et al., 2001; Peltier, 1998). Second, the dynamics and stability of ice sheets depend significantly on the uplift rate of the underlying bedrock as ice sheets melt (Gomez et al., 2018). This process may play an important role in assessing the fate of West Antarctica ice sheets that have been losing their mass at an alarming rate. Third, modeling solid-Earth's response to surface loading and comparing the model predictions with relevant observations (e.g., deglaciation-induced sea level change and crustal displacements) is the primary way to infer mantle viscosity and rheology (Lambeck et al., 2017; Milne et al., 2001; Peltier et al., 2015) which is essential to studies of mantle dynamics and Earth's evolution (Zhong et al., 2007).

The solid Earth's response to forcing is determined by solving the equations of motion with relevant rheological properties of the mantle and crust. Under the assumption of spherical symmetry in elasticity and viscosity structure (i.e., only 1-D or radial dependence), analytical solutions to the equations of motion are available in spectral or normal mode domains for the displacement, strain and stress (Longman, 1963; Takeuchi, 1950; Wu and Peltier, 1982). However, the Earth's mantle structure has significant lateral variations as demonstrated by seismic imaging studies on both global (Ritsema et al., 2011; French and Romanowicz, 2015; Tromp, 2020) and regional (e.g., Lloyd et al., 2020) scales. Because of the large sensitivity of mantle viscosity to temperature, lateral variations in mantle viscosity are expected to exceed several orders of magnitude (e.g., Paulson et al., 2005; Ivins et al., 2023). For the mantle with fully 3-D elastic and viscosity structures, numerical solution methods are required to solve the equations of motion. The necessity for numerical solution methods has become increasingly more evident as more observations

of higher quality (e.g., Bevis et al., 2012) become available to place constraints on the models. In recent years, numerous numerical methods have been developed, including a spectral-finite element (Martinec, 2000; Klemann et al., 2008; Tanaka et al., 2011; Bagge et al., 2021), finite element (Zhong et al., 2003, 2022; Paulson et al., 2005; A et al., 2013; Wu, 2004; Huang et al., 2023; Weerdesteijn et al., 2023), and finite volume (Latychev et al., 2005) methods. Some of them (Bagge et al., 2021; Klemann et al., 2008; Martinec, 2000; Paulson et al., 2005; Weerdesteijn et al., 2023; Wu, 2004; Zhong et al., 2003, 2022) assumed an incompressible rheology in their models while others included the compressibility.

The CitcomSVE package is a finite element modeling package for solving load-induced viscoelastic deformation problems in a 3-D spherical shell, a spherical wedge or a Cartesian domain. CitcomSVE solves the sea level equation and incorporates the effects of polar wander and apparent motion of center of the mass (Zhong et al., 2003, 2022; A et al., 2013; Paulson et al., 2005). CitcomSVE works for 3-D viscoelastic mantle structures with either linear or non-linear viscosity. It works efficiently on massively parallel computers (>6,000 CPU cores), making it feasible for routine high-resolution GIA modeling calculations (~30 km horizontal resolution on the Earth's surface and ~10 km vertical resolution in the upper mantle). CitcomSVE, developed over the last two decades, has been used in GIA studies for both the incompressible (Zhong et al., 2003, 2022) and compressible (A et al., 2013) mantle with temperature- (Paulson et al., 2005) and stress-dependent viscosity (Kang et al., 2022), and in tidal deformation studies for the Moon (Zhong et al., 2012; Qin et al., 2014; Fienga et al., 2024). CitcomSVE was built from the mantle convection modeling package CitcomS (Zhong et al., 2000, 2008) by replacing viscous rheology and Eulerian formulation in CitcomS with viscoelastic rheology and Lagrangian formulation, respectively (Zhong et al., 2003, 2022), and they share many common features including the grid. The spherical shell of the mantle is divided into 12 caps of similar size, and each cap is further divided into a grid of cells (i.e., elements) of similar size with eight displacement nodes per element (Zhong et al., 2000; 2008; 2022). This design of finite element grid is suited for parallel computing, as discussed in Zhong et al., (2008). An important feature of this grid is its approximately uniform resolution from the polar to

93 equatorial regions (Zhong et al., 2000; 2003), different from some of the other numerical GIA codes (e.g.,
94 Martinec, 2000; Klemann et al., 2008; Wu, 2004; van der Wal et al., 2013; Huang et al., 2023). However,
95 CitcomSVE also supports regional grid refinement to achieve higher horizontal resolutions in interested
96 regions.

97 Recently, Zhong et al. (2022) presented an expansive set of benchmark calculations for single
98 harmonic surface loading, tidal loading, and glaciation and deglaciation loading history (i.e., ICE-6G) for
99 a significantly improved version of CitcomSVE-2.1. Compared with previous versions of CitcomSVE that
100 only used 12 CPU cores (e.g., Zhong et al., 2003; A et al., 2013), the most important improvement with
101 CitcomSVE-2.1 is its capability of efficiently using any large number of CPU cores (e.g., > 6000 CPU cores
102 as in Zhong et al., (2022)). CitcomSVE-2.1 has also become the first GIA modeling software package that
103 is open source and publicly available via GitHub (Zhong et al., 2022). However, CitcomSVE-2.1 is for an
104 incompressible mantle, which limits its applications, especially for studies on GIA-induced horizontal
105 crustal motions and where realistic elastic structure (e.g., PREM) is necessary (Mitrovica et al., 1994).

106 This paper presents CitcomSVE-3.0, an extension of CitcomSVE-2.1, by incorporating mantle
107 compressibility as in A et al. (2013). While the numerical techniques for implementing mantle
108 compressibility are the same as in A et al. (2013), this paper includes significantly more detailed benchmark
109 calculations and an improved sea level equation solver. With its public availability via GitHub and efficient
110 parallel computing, CitcomSVE-3.0 offers the scientific community a powerful computational tool for
111 solving an important class of geodynamic questions, including the GIA and tidal deformation for Earth's
112 mantle with realistic viscosity and rheology. The paper is organized as follows. The next section describes
113 the governing equations for dynamic loading problems and numerical methods. Section 3 defines
114 benchmark problems and presents benchmark results, including error analyses. Discussions and
115 conclusions are given in the final section.

2. Governing Equations and Numerical Methods

2.1. Governing Equations and Viscoelastic Properties of the Mantle

The governing equations for load-induced deformation are derived from the conservation laws of mass and momentum and Newton's law of gravitation, together with viscoelastic constitutive equation (Wu and Peltier, 1982; A et al., 2013):

$$\rho_1^E = -(\rho_0 u_i)_{,i}, \tag{1}$$

$$\sigma_{ij,j} + \rho_0 \phi_{,i} - (\rho_0 g u_r)_{,i} - \rho_1^E g_i + \rho_0 V_{a,i} = 0, \tag{2}$$

$$\phi_{,ii} = -4\pi G \rho_1^E, \tag{3}$$

where ρ_1^E is the Eulerian density perturbation, ρ_0 is the unperturbed mantle density and is horizontally homogenous (i.e., radially layered), u_i represents the displacement vector with u_r being in the radial direction, σ_{ij} is the stress tensor, ϕ is the perturbation of gravitational potential due to deformation, V_a is the applied potential (e.g., rotational and tidal potentials) when applicable, g_i is the gravitational acceleration with $g = \sqrt{g_i g_i}$, and G is the gravitational constant. The equations are written in an indicial notation such that $A_{,i}$ represents the derivative of variable A with respect to coordinate x_i, and repeated indices indicate summation.

Both the surface (at radius $r = r_s$) and core-mantle boundary (CMB) ($r = r_b$) experience zero shear force but are subjected to normal forces

$$\sigma_{ij} n_j = -\sigma_o n_i, \qquad \text{for } r = r_s, \tag{4}$$

$$\sigma_{ij} n_j = (-\rho_c \phi + \rho_c g u_r) n_i, \qquad \text{for } r = r_b, \tag{5}$$

where σ_o represents the pressure loads at the surface (e.g., glacial loads) as a function of time and space, ρ_c is the density of the core, and n_i represents the normal vector of the surface or CMB. The boundary conditions at the CMB consider the self-gravitational effect for a fluid incompressible core (e.g., Zhong et

al., 2003). Except for this CMB boundary condition, the core is not considered explicitly in our numerical formulation. With such boundary conditions of forces, both the surface and CMB can deform dynamically in both horizontal and radial directions.

CitcomSVE has implemented formulations for both incompressible (e.g., Zhong et al., 2003; 2022) and compressible (A et al., 2013) continuum. In this study for compressible continuum, we follow the formulation by A et al., (2013). Here, we will only provide a general description for the formulation and numerical analyses. The details for the compressibility-related topics and numerical analyses of CitcomSVE can be found in A et al., (2013) and Zhong et al., (2022), respectively. Note that CitcomSVE also incorporates the effects of polar wander and apparent motion of the center of mass (i.e., degree-1 deformation), and uses a reference frame centered at the center of mass including the mass of loads with no net rotation of the mantle and crust (Zhong et al., 2022; Paulson et al., 2005; A et al., 2013).

The Earth's mantle is considered as a compressible Maxwell solid, and the constitutive equation can be written as (e.g., Wu and Peltier, 1982)

$$\dot{\sigma}_{ij} + \frac{\mu}{\eta}(\sigma_{ij} - \frac{1}{3}\sigma_{kk}\delta_{ij}) = \lambda\dot{\varepsilon}_{kk}\delta_{ij} + 2\mu\dot{\varepsilon}_{ij}, \quad (6)$$

where η is the viscosity, λ and μ are the Lamé parameters, and δ_{ij} is the Kronecker delta function. The strain ε_{ij} is related to the displacement by $\varepsilon_{ij} = \frac{1}{2}(u_{i,j} + u_{j,i})$. Both Lamé parameters ($\lambda$ and μ) and viscosity η can be fully 3-dimensional in CitcomSVE models to represent the effects of temperature, composition and stress on mantle mechanical properties (e.g., Zhong et al., 2003; A et al., 2013; Kang et al., 2022). However, for this benchmark study, we will only consider radially layered λ, μ, and η.

2.2. Numerical Analysis

A finite element method is employed in CitcomSVE to solve the governing equations (1)-(3) for load-induced displacement under boundary conditions (4)-(5) with a Maxwell rheology (6) (Zhong et al., 2003; 2022; A et al., 2013). However, before presenting a weak form of the governing equations for the

finite element analysis, it is necessary to introduce an incremental displacement formulation, re-formulate the time-dependent rheological equation (i.e., equation 6), and discuss solution strategies for the gravitational potential that results from mass anomalies associated with mantle deformation via the Eulerian density perturbation ρ_1^E as controlled by the Poisson's equation (i.e., equation 3).

Define u_i^n and u_i^{n-1} as displacements at times t and t-Δt, respectively, where superscripts *n* and *n-1* represent time steps. Incremental displacement at time *t*, v_i^n, is defined as $v_i^n = u_i^n - u_i^{n-1}$ and it is related to incremental strain $\Delta\varepsilon_{ij}^n$ as

$$\Delta\varepsilon_{ij}^n = \frac{1}{2}(v_{i,j}^n + v_{j,i}^n). \quad (7)$$

Rheological equation (6) is discretized in time by integrating it from time t-Δt to t, and stress tensor at time t, σ_{ij}^n, is given in terms of incremental strain $\Delta\varepsilon_{ij}^n$, stresses at time step *n-1* (i.e., pre-stress), and material properties as (A et al., 2013; Zhong et al., 2003),

$$\sigma_{ij}^n = \tilde{\lambda}\Delta\varepsilon_{kk}^n\delta_{ij} + 2\tilde{\mu}\Delta\varepsilon_{ij}^n + \tau_{ij}^{pre}, \quad (8)$$

where $\tau_{ij}^{pre} = (1 - \frac{\Delta t}{2\alpha})/(1 + \frac{\Delta t}{2\alpha})\sigma_{ij}^{n-1} + \frac{\Delta t}{3\alpha}/(1 + \frac{\Delta t}{2\alpha})\sigma_{kk}^{n-1}\delta_{ij}$, $\tilde{\lambda} = [\lambda + (\lambda + \frac{2\mu}{3})\frac{\Delta t}{2\alpha}]/(1 + \frac{\Delta t}{2\alpha})$, $\tilde{\mu} = \mu/(1 + \frac{\Delta t}{2\alpha})$, $\alpha = \eta/\mu$ is the Maxwell time, and τ_{ij}^{pre} represents the pre-stress at timestep n-1 (A et al., 2013).

The Poisson's equation for gravitational potential anomaly ϕ (i.e., equation 3) is solved in a spherical harmonic domain for mass anomalies associated with the Eulerian density perturbation ρ_1^E and the loads (e.g., ice and water loads). For a compressible mantle, ρ_1^E exists throughout the mantle and crust (see equation 1), and it is necessary to express ρ_1^E at each depth in terms of spherical harmonic degree *l* and order *m*. The gravitational potential anomaly at radius *r* and time *t* and at degree *l* and order *m*, $\phi_{lm}(r,t)$, can be related to mass anomalies via Green's function formulation (e.g., A et al., 2013; Zhong et al., 2008). The solution of $\phi_{lm}(r,t)$ needs to recast to finite element grid points in solving the equation of motion

(i.e., equation 2). It should be pointed out that the transformation for gravitational potential anomalies ϕ between the spherical harmonic domain and the spatial domain is computationally rather expensive.

We now present the weak form of the equation of motion (i.e., equation 2) for the compressible mantle as (A et al., 2013)

$$\int_\Omega w_{i,j}\left[\tilde{\lambda} v_{k,k}\delta_{ij} + \tilde{\mu}\left(v_{i,j} + v_{j,i}\right)\right]dV - \int_\Omega \rho_0 g(w_{i,i}v_r + w_r v_{i,i})dV + \sum_l \int_S w_r \Delta\rho_l g v_r dS_l$$

$$= -\int_\Omega w_{i,j}\tau_{ij}^{pre}dV + \int_\Omega \rho_0 g(w_{i,i}U_r + w_r U_{i,i})dV - \int_\Omega w_{i,i}\rho_0\phi dV$$

$$+\sum_l \int_{S_l} w_r(\Delta\rho_l\phi - \Delta\rho_l g U_r + \rho_0 \mathrm{V}_a)dS_l - \int_S w_r\sigma_0 dS, \quad (9)$$

where integration domain Ω, S_l, and S are for the volume, the horizontal surface at some depth with the *l-th* density boundary, and the Earth's surface, respectively, w_i is the displacement weighting function, U_i is the cumulative displacements at the previous time step, V_a is the applied potential which is only relevant for tidal loading, and σ_0 is the surface load. Note that the gravitational potential anomalies ϕ in equation (9) depend on the unknown incremental displacement v_i. We decompose ϕ into $\phi = \Phi + \Delta\phi(v_i)$, where Φ is the total potential at the previous time step and $\Delta\phi(v_i)$ is the incremental potential determined by v_i and other incremental mass anomalies at the current time step.

Equation (9) is discretized onto a set of finite element grids to form a system of matrix equations with unknown vectors of incremental displacement $\{V\}$.

$$[K]\{V\} = \{F_0\} + \{F(\Delta\phi)\}, \quad (10)$$

where $[K]$ is the stiffness matrix, $\{F_0\}$ is the force vector representing contributions from the previous time step, and $\{F(\Delta\phi)\}$ represents contributions from the incremental potential $\Delta\phi$ which depends on the unknown displacement $\{V\}$ and other incremental mass anomalies. An iteration scheme is applied to equation (10) to obtain a convergent solution for $\{V\}$ (Zhong et al., 2003).

Matrix equation (10) is solved with a parallelized full multigrid method (Zhong et al., 2000; 2008). The general solution strategy in CitcomSVE follows an iterative scheme that can be summarized as (Zhong et al., 2003; A et al., 2013):

1) At a given time t, $\{F_0\}$ is first evaluated using pre-stress τ_{ij}^{pre}, gravitational potential Φ and displacements U_i at the previous time step, t-Δt, and set $\{F\} = \{0\}$.
2) Solve equation (10) using the full multigrid method for incremental displacements $\{V\}$, using $\{F_0\}$ and $\{F\}$.
3) Compute incremental potential $\Delta\phi_{lm}(r,t)$ by solving equation (3) with the incremental displacements from step 2, and then re-evaluate $\{F\}$. Go back to step 2 to solve for $\{V\}$ again.
4) Repeat steps 2 and 3, until $\{V\}$ converges to a given threshold error tolerance (specified by users and is 0.3% in this study). Then go back to step 1 to march forward in time.

In the implementation of equation (10) in CitcomSVE, all the variables and parameters are normalized to be dimensionless, and the outputs are also dimensionless. CitcomSVE uses the following normalization scheme. The coordinates x_i and displacements u_i and v_i are all normalized by the radius of a planet, r_s. The time is normalized by a reference mantle Maxwell time $\alpha = \eta_r/\mu_r$, where η_r and μ_r are the reference mantle viscosity and shear modulus, respectively. η_r is also used to normalize mantle viscosity and μ_r is used to normalize elastic moduli, stress tensor and pressure, while the density is normalized by reference density ρ_0. Gravitational potential and centrifugal potential are normalized by $4\pi G\rho_0 r_s^2$, and the geoid anomalies are normalized by $4\pi G\rho_0 r_s^2/g$. Any other variables can be normalized by combining the abovementioned scales. However, model input parameters are defined by users as dimensional values. For example, 3-D mantle viscosity and elasticity models are given by users in separated files on a regular grid (e.g., 1°x1° grid) at different depths. CitcomSVE reads these parameters from the files, normalizes them, and interpolates them onto the finite element grids. Along with public releases of CitcomSVE 2.1 and 3.0 on GitHub, a user manual is available to describe the usage of the code and the input and output files.

We now finish this section by highlighting the two main differences between incompressible and compressible models in CitcomSVE (i.e., versions 2.1 versus 3.0). First, the compressible model presented here does not include the pressure term which is a key component of incompressible models. The absence of the pressure term simplifies the matrix equation (i.e., equation 10) and its solution procedure, but for the incompressible model, a two-level Uzawa algorithm is needed to solve for both the pressure and displacement. Second, mantle compressibility causes mass anomalies or Eulerian density perturbation ρ_1^E throughout the mantle, while for an incompressible mantle, mass anomalies only exist at the surface and CMB. Consequently, the compressible model is computationally more expensive, particularly for calculating the gravitational potential anomalies.

2.3. Sea Level Change and Sea Level Equation

Understanding and modeling sea level change is important for GIA studies. Sea level change is controlled by ice volume change and GIA-induced vertical crustal motion and gravitational potential change. Therefore, the records of sea level change provide essential constraints on GIA processes, including ice volume change and mantle viscosity. Moreover, sea level change acts as a change of load on the surface, affecting solid-Earth deformation and gravitational potential. Modeling the GIA processes, one of the major applications of the CitcomSVE package, requires an accurate sea level equation that describes the sea level change in this process. A major improvement of CitcomSVE 3.0 over its previous versions is on modeling sea level changes, and a detailed description is given in this section.

The original sea level equation formulated by Farrell and Clark (1976) provides an elegant way to incorporate the sea level change into GIA models and can explain the diverging pattern of sea level change in different regions (e.g., near or far away from former ice sheets). However, the simplified formulation by Farrell and Clark ignored several factors affecting the accuracy of sea level change modeling. One key simplification is on the time-dependent ocean-continent function that describes the ocean and continent distribution, which was assumed to be constant through time in their formulation. The ocean area has varied by several percent since the last glacial maximum because of the shoreline evolution induced by sea level

rise or fall (Fig. S1). Accounting for the time-dependent ocean-continent function requires modifications of the sea level equation and affects the predicted sea level change by tens of meters for some regions compared to that based on Farrell and Clark's formulation (Kendall et al., 2005). Kendall et al. (2005) provides a modified sea level equation that accounts for the time-dependent ocean function, in which the variation of ocean area is mainly attributed to two factors: 1) formation or melting of marine ice sheets (i.e., ice sheets that lie below sea level), 2) the evolution of shorelines related to the sloping bathymetry and local sea level change. In previous versions of CitcomSVE, we only considered the variation of ocean function related to marine ice sheets (A et al., 2013; Zhong et al., 2022). In our new formulation, the sea level equation is modified to follow the formulation of Kendall et al. (2005). The new sea level equation can be summarized as follows:

$$L_0(\theta,\phi,t) = [N(\theta,\phi,t) - U(\theta,\phi,t) + c(t)]O(\theta,\phi,t)$$

$$-T_0(\theta,\phi)[O(\theta,\phi,t) - O(\theta,\phi,t_0)]\,, \tag{11}$$

Where t is the time with t_0 as the initial time (i.e., the onset of loading), θ and ϕ are co-latitude and longitude, respectively, L_0 is the change in sea level relative to the initial stage, N and U are GIA-induced geoid anomalies and surface radial displacement, O is ocean function (1 for ocean and 0 elsewhere), T_0 is initial topography at t_0, and c is introduced for the conservation of water mass and is defined as:

$$c(t) = \frac{1}{A_0(t)}\{-\frac{M_{ice}(t)}{\rho_w} - \int [N(\theta,\phi,t) - U(\theta,\phi,t)]O(\theta,\phi,t)dS$$

$$+\int T_0(\theta,\phi)[O(\theta,\phi,t) - O(\theta,\phi,t_0)]dS\}, \tag{12}$$

where M_{ice} is the ice mass change relative to the initial stage (i.e., t_0), A_0 is the ocean area at time t, ρ_w is water density, N and U are relative to t_0, and the integral is for the surface of Earth. Following Kendall et al. (2005), a check for grounded ice is incorporated using the criterion that at any location with topography T and ice of thickness I and of density ρ_i, the ice is considered as ground ice if $I\rho_i > -T\rho_w$. Only grounded ice is treated as ice load, whereas regions with non-grounded ice (i.e., floating ice) are

277 treated as oceans. Note that regions with topography $T<0$ and without grounded ice are considered as
278 ocean.

279 The sea level equation can only be solved iteratively for three reasons: 1) the calculation of
280 geoid/displacement and ocean load depends on each other (eq. 4 and eq. 11), 2) the ocean load also depends
281 on the ocean function, and 3) the unknown initial topography T_0 needs to be determined iteratively to keep
282 the modeled present-day topography consistent with the observed present-day topography. A normal single
283 complete GIA modeling uses pre-determined initial topography T_0 and time-dependent ocean function $O(t)$
284 to iteratively determine $N(t), U(t)$, and $L_0(t)$ for each time step t from t_0 to the present day, where the
285 iteration for each step is considered converged when the changes of potential and/or displacement are
286 smaller than a certain threshold. The algorithm for solving the sea level equation in Kendall et al., (2005)
287 adds an outer layer of iterations to the single complete GIA modeling. In the outer layer iteration
288 calculations, at the end of each single complete GIA model run, time-dependent ocean function $O(t)$ and
289 paleo-topography including initial topography T_0 are updated using newly calculated $U(t)$ and $N(t)$ and
290 the present-day topography, and the updated T_0 and $O(t)$ are then used for the next GIA model run. The
291 iteration procedure continues until the initial topography converges. In practice, the model results would
292 not be altered significantly beyond the second outer iteration. However, there are noticeable differences in
293 results (e.g., modeled RSL histories) between the first and second outer iterations for some sites following
294 the algorithm developed by Kendall et al. (2005).

295 We implemented the algorithm developed by Kendall et al. (2005) in our semi-analytic code (e.g.,
296 A et al., 2013) and produced consistent results with Kendall et al. (2005). However, running two or three
297 outer iterations where each iteration is a complete GIA model run of a glacial cycle is computationally
298 expensive, especially for numerical modeling such as in CitcomSVE, and it would be more efficient if the
299 results from the first outer iteration (i.e., a single complete GIA model run) can be sufficiently accurate. In
300 Kendall's algorithm, the time-dependent ocean function $O(t)$ for the first outer iteration is constructed
301 using fixed shorelines same as that of the present day, except that the extent of oceans may be limited by

the existence of grounded marine ice sheets. However, we found that the first iteration may produce much improved solutions if $O(t)$ for the first outer iteration is constructed by calculating the change of ocean area (i.e., ocean-continent transitions) based on ice volume change (i.e., M_{ice}) and the present-day topography (bathymetry), assuming barystatic sea level change on a rigid Earth (i.e., no radial surface displacement). The ocean function generated in this way generally captures the shoreline evolution for regions experiencing ocean-land transition, and this approximation makes it easy to derive the time-dependent ocean function for any given ice model. In the supplementary material, we show the effectiveness of this single outer iteration method using the improved ocean function in both our semi-analytic solution method and CitcomSVE-3.0.

3. Example Calculations and Benchmark Results

Two example problems solved using CitcomSVE 3.0 are presented here. They are: 1) loading problems with a single spherical harmonic in space (spectral load) and step-function (i.e., Heaviside function) in time as either surface load or tidal load; 2) GIA problems with ICE-6G_D ice history model. For each example problem, the elastic and viscosity structures are chosen to be dependent only on the radius (i.e., 1-D) so that CitcomSVE solutions can be benchmarked against semi-analytical solutions. The following benchmarks largely follow the approaches of Zhong et al. (2022).

3.1. Spectral load with step-function in time.

3.1.1. Definition of the spectral loading problem.

For the first example problem, we consider a surface load σ_0 (see equation 4) corresponding to amplitude of topographic variation d with density ρ_0 at a single harmonic function in space (ranging from degree 1 to degree 64) and step-function in time:

$$\sigma_0(t,\theta,\varphi) = \rho_0 g d \cos(m\varphi)\, p_{lm}(\theta) H(t) = \rho_0 g d \bar{P}_{lm}(\theta,\varphi) H(t), \quad (13)$$

where H(t) is the Heaviside function (i.e., $H(t)$=1 for $t \geq 0$; $H(t)$=0 otherwise) and $\bar{P}_{lm}(\theta,\varphi) = \cos(m\varphi)\, p_{lm}(\theta)$ is the cosine part of spherical harmonic functions in the real form. Note that only cosine

terms of longitudinal dependence are considered for simplicity. A small amplitude of the load height is used to avoid large grid deformations. We assume an ocean-free Earth for this example and ignore any sea-level-related calculations. The density and Lame parameters for lithosphere and mantle are from PREM, except that for the crust layer those properties are replaced to be same as the underlying mantle, and the viscosity structure is from VM5a (Peltier et al, 2015). See Table 1 for model parameters. Time-dependent surface 3-D displacements and gravitational potential anomalies are computed using the newly updated CitcomSVE and compared with those from semi-analytical solutions (Han and Wahr, 1995; Paulson et al., 2005; A et al., 2013). The results are presented in terms of load Love numbers h_l, k_l, and l_l at harmonic degree l for radial displacement, gravitational potential, and horizontal displacement, respectively. The definitions of load Love numbers in the context of CitcomSVE calculations are given in equations 37-41 of Zhong et al., (2022). Similarly, one tidal loading benchmark with (2,0) tidal force is conducted (named l2m0T in Table 2, where T stands for tidal loading). The definitions of tidal force and tidal Love numbers follow Zhong et al., (2022, Eq. 44-47).

Table 1. Model parameters for benchmarks

Model parameters	value
Earth radius r_s	6371 km
CMB radius r_b	3485.5 km
Reference density ρ_0	4400 kg/m^3
Core density	10895.62 kg/m^3
Water density ρ_w	1000 kg/m^3
Ice density ρ_i	917.4 kg/m^3
Reference shear modulus μ	1.4305x10^{11} Pa
Modified Fluid Love number $k_{2f}(1+\delta)$	0.9521091
Mantle reference viscosity η	2x10^{21} Pa·s
Reference Maxwell time (η/μ)	443 years
Gravitational acceleration g	9.82 m·s^{-2}
VM5A viscosity model:	

The surface to 60 km depth	10^{26} Pas
60 to 100 km depth	10^{22} Pas
100 to 670 km depth	4.853×10^{20} Pas
670 to 1170 km	1.5048×10^{21} Pas
1170 km to CMB	3.095×10^{21} Pas

339

340

341 3.1.2. Benchmark results.

342 We have computed a set of model cases using CitcomSVE for four numerical resolutions and six
343 loading harmonics. Seven different loading harmonics are included for (1,0), (2, 0), (2,1), (4, 0), (8, 4), (16,
344 8), and (64,32) where the first and second numbers in parenthesis (l, m) indicate spherical harmonic degree
345 l and order m, respectively. For the loading at (2,1) harmonic, the polar wander effect is considered. For
346 most cases, four different numerical resolutions of R1-R4 are for 12x(32x32x32), 12x(64x64x64),
347 12x(64x96x96) and 12x(64x128x128), respectively, where the first number, 12, indicates the number of
348 spherical caps that the spherical surface is divided into, and the subsequent numbers indicate the number of
349 elements in the radial and two horizontal directions in each cap (Zhong et al., 2022). Each case is named
350 by its loading harmonic and numerical resolution; for example, case l2m0_R1 corresponds to the case where
351 the loading harmonic is (2, 0) and the resolution is R1. For case l16m8, an additional calculation with
352 resolution 12x(80x128x128) is included (i.e., l16m8_R5). For case l64m32, which has a much shorter
353 loading wavelength and requires higher numerical resolutions, four calculations with resolutions of R5-R8
354 are included (Fig. 1) where R6-R8 are 12x(80x192x192), 12x(80x256x256), and 12x(96x256x256),
355 respectively. Grid size in the vertical direction is not uniform since grids get refined vertically in the upper
356 mantle and lithosphere for each model. For cases with 64 elements in the vertical direction (R2, R3 and
357 R4), the vertical resolutions are about 20 km, 40 km, and more than 50 km in the lithosphere, upper mantle
358 and lower mantle, respectively. R5, with a total of 80 elements in the vertical direction, has vertical
359 resolutions of ~ 10 km in the lithosphere and ~ 20 km in the upper mantle, whereas R8 is ~ 7 km in the

lithosphere and ~ 10 km in the upper mantle. Each case is computed for 40 Maxwell times (i.e., 40α or non-dimensional time of 40), using a non-dimensional time increment of 0.2. Figure 1 shows $h_l(t)$, $k_l(t)$, and $|l_l(t)|$ for cases with different loading harmonics and numerical resolutions, together with semi-analytical solutions. Table 2 shows both numerical and analytical results of these Love numbers at t=0 and 40 for a selected set of cases (supplementary Table S1 for all the cases). Solutions at t=0 represent the elastic responses of Earth, and the magnitudes of those Love numbers generally increase with time due to viscous relaxation and finally reach nearly stable states after certain time periods (Fig. 1).

Table 2: Comparison of Load Love Numbers h_l, k_l, and l_l Between CitcomSVE and Semi-Analytical Solutions

Case[a]	$h_l(0)$[b]	$k_l(0)$	$\|l_l(0)\|$	$h_l(40)$	$k_l(40)$	$\|l_l(40)\|$
l1m0_R4	-1.2546(-1.2543)	-1.0000(-1.0000)	0.8864(0.8866)	-1.4968(-1.4964)	-1.0000(-1.0000)	1.9101(1.9090)
l2m0_R4	-0.9574(-0.9577)	-0.3038(-0.3041)	0.0203(0.0200)	-2.4066(-2.4066)	-0.9392(-0.9396)	0.8229(0.8216)
l2m1_R4	-0.3056(-0.3058)	1.0948(1.0944)	0.1118(0.1118)	0.6178(0.6151)	2.2003(2.1973)	0.1891(0.1884)
l4m0_R4	-1.0247(-1.0251)	-0.1341(-0.1342)	0.0569(0.0568)	-4.4395(-4.4402)	-0.9410(-0.9416)	0.3423(0.3411)
l8m4_R4	-1.2372(-1.2376)	-0.0772(-0.0772)	0.0303(0.0302)	-8.8084(-8.8405)	-0.9563(-0.9605)	0.0977(0.0958)
l16m8_R4	-1.6825(-1.6868)	-0.0573(-0.0574)	0.0228(0.0229)	-17.535(-17.847)	-0.9530(-0.9726)	0.0435(0.0479)
l16m8_R5	-1.6805(-1.6868)	-0.0572(-0.0574)	0.0228(0.0229)	-17.623(-17.847)	-0.9579(-0.9726)	0.0464(0.0479)
l64m32_R7	-2.3469(-2.3851)	-0.0227(-0.0231)	0.0109(0.0111)	-21.4626(-22.5878)	-0.2901(-0.3084)	0.1034(0.1081)
l2m0T_R4[c]	0.6074 (0.6076)	0.3033(0.3035)	0.0855(0.0855)	1.8611(1.8609)	0.9215(0.9202)	0.6217(0.6229)

[a]Case names follow this notation: l1m0 stands for loading harmonic for l=1 and m=0. All CitcomSVE solutions in this table are for resolution R4 (12x64x128x128), except for l16m8_R5 with a resolution of 12x80x128x128 (R5) and l64m32_R7 with resolution 12x80x256x256 (R7).

[b]Load Love numbers are provided at 0 and 40 Maxwell time. Each entry includes semi-analytical solutions inside parentheses and CitcomSVE solutions outside parentheses.

[c]l2m0T: Tidal Love numbers for a Heaviside (2,0) tidal load. Each entry includes semi-analytical solutions inside parentheses and CitcomSVE solutions (with a resolution of 12x64x128x128) outside parentheses.

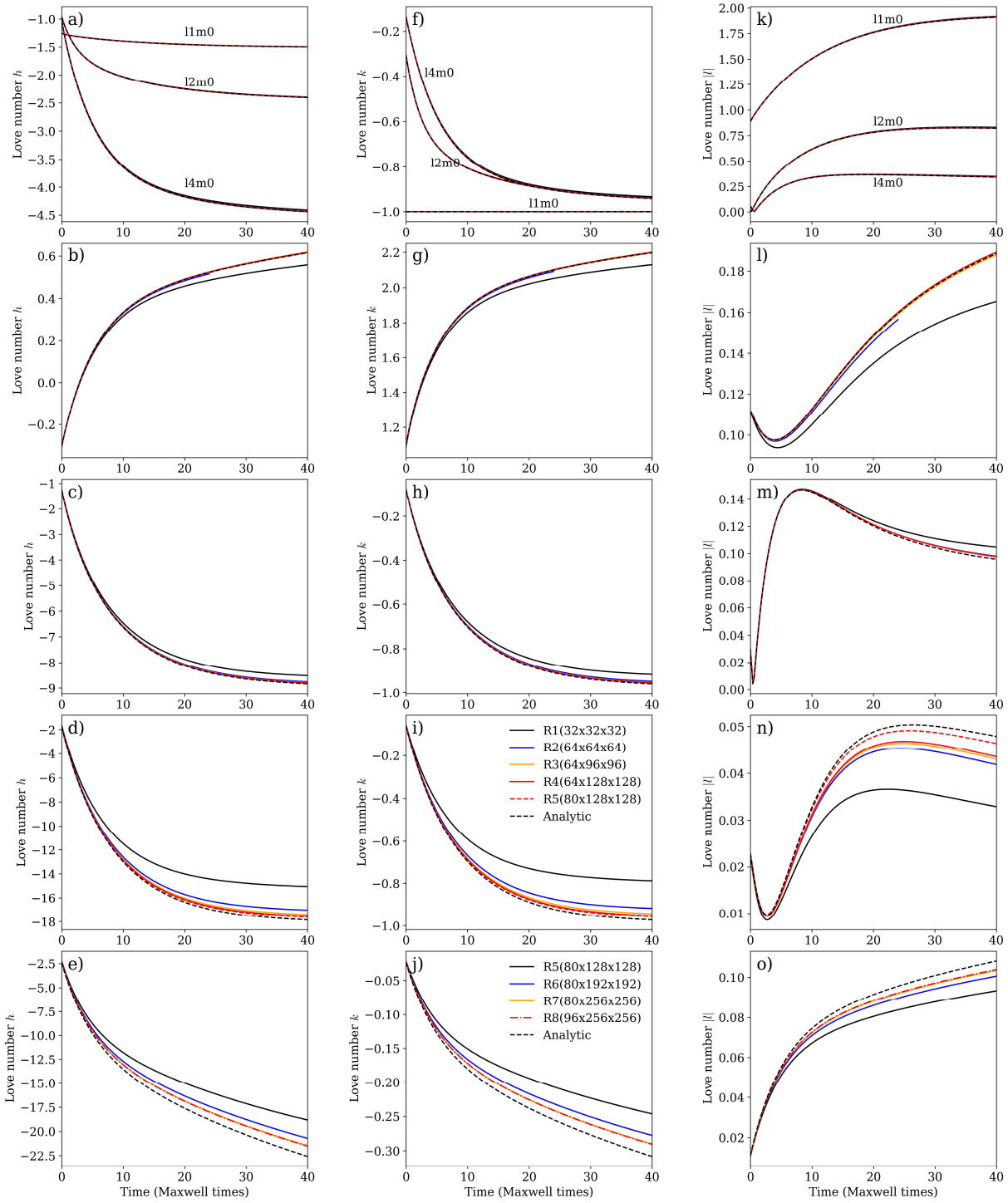

Figure 1. Love numbers h, k and l for cases with different loading harmonics from CitcomSVE and analytical solutions. The first, second, and third columns are for Love number h, k and $|l|$ (i.e., the absolute values of Love number l), respectively. The first row is for loading harmonics l1m0, l2m0 and l4m0. The following rows are for loading harmonics l2m1, l8m4, l16m8, and l64m32, respectively. Each loading case

has solutions from four different spatial resolutions (R1-R4), except that loading case l16m8 has an additional calculation with resolution R5, and cases with l64m32 (i.e., the last row) have resolutions from R5 to R8. Note the legend in panel i is used for all panels except those in the last row.

The comparison shows a good agreement between numerical solutions and semi-analytical solutions. For long-wavelength loadings (e.g., l1m0, l2m0, l2m0T, and l4m0), numerical solutions at different resolutions (R1-R4) are nearly identical to semi-analytical solutions, as shown in Figure 1. However, for l2m1 cases with the polar wander effect, resolution R1 shows significant numerical errors, whereas calculations with higher resolutions (R2-R4) deliver a remarkable fit to the semi-analytical solution, suggesting that polar wander is more challenging to compute in numerical models (e.g., Paulson et al., 2005; A et al., 2013; Zhong et al., 2022). For shorter wavelengths (such as l8m4, l16m8, and l64m32), low-resolution numerical results differ noticeably from semi-analytical solutions. As the numerical resolution increases, the results match the semi-analytical solutions much more closely (Figure 1). For l16m8, case R5 significantly reduces errors in l_l compared to R4. Note that R5 has a higher vertical resolution in the upper mantle but the same horizontal resolution as R4 (Fig.1 and Table 2). For case l64m32, increasing vertical resolution does not reduce the misfit from R7 to R8, indicating that horizontal resolution is the controlling factor. Note that the load Love number for horizontal displacement is presented as $|l_l(t)|$, because CitcomSVE only conveniently determines $l_l^2(t)$ (Zhong et al., 2022), although it is possible to determine the l_l based on vector spherical harmonic decomposition of horizontal surface motion (Wu and Peltier 1982).

We determine numerical errors by computing amplitude and dispersion errors (e.g., Zhong et al., 2003; A et al., 2013; Zhong et al., 2022). Amplitude error ε_a and dispersion error ε_d are computed using the following equations (Zhong et al., 2022):

$$\varepsilon_a = \frac{\int_0^T |S_n(l_0,m_0,t) - S_{sa}(l_0,m_0,t)|dt}{\int_0^T |S_{sa}(l_0,m_0,t)|dt}, \quad (14)$$

$$\varepsilon_d = \frac{\int_0^T \max\left[|S_n(l,m,t)|\right]dt}{\int_0^T |S_{sa}(l_0,m_0,t)|dt}, \quad (15)$$

where l_0 and m_0 represent the loading harmonic degree and order, S_n and S_{sa} are solutions of load Love numbers from CitcomSVE and semi-analytical methods, respectively, T is the total model time (i.e., 40), and in equation (15) for the dispersion error, max represents the maximum value for all the non-loading harmonic degrees l and orders m. The response should only occur at the loading harmonic for the spherically symmetric mantle structure considered here. Therefore, amplitude error ε_a measures the accuracy at the loading harmonic and dispersion error ε_d measures the accuracy at other harmonics. Note that the errors defined in equations (14) and (15) are similar to norm-1 errors.

Figure 2 shows the amplitude errors of load Love numbers as a function of horizontal numerical resolution (i.e., the horizontal grid size ranging from ~200 km to ~50 km at the surface for resolutions R1-R4) for all cases except for case l64m32 which has a different range of horizontal resolutions. For most of the calculations with different loading harmonics, the amplitude errors decrease with decreasing horizontal grid size with a slope of close to 2 in the log-log plot of Figure 2, especially for Love numbers h_l and k_l. This suggests that the error is roughly proportional to the square of the grid size, aligning with the expected second-order accuracy for trilinear elements in CitcomS (e.g., Zhong et al., 2008). It is worth noting that from R1 to R4, the increase in vertical resolution is not proportional to the increase in horizontal resolution, which may cause the slope in Figure 2 to deviate from 2. Figure 2 shows that with a horizontal resolution of ~ 50 km, the accuracy of CitcomSVE is better than 0.1% up to spherical harmonics of degree 4 and better than 2% up to spherical harmonics of degree 16 in terms of Love numbers h_l and k_l. For Love number l_l, the errors are slightly larger than that for h_l and k_l. Compared to the benchmark results of CitcomSVE-2.1 (Zhong et al., 2022), the errors presented here are generally larger for cases with the same resolutions, which is understandable considering that CitcomSVE-3.0 solves for models with higher complexity (i.e., the internal density variations caused by compressibility and density discontinuities).

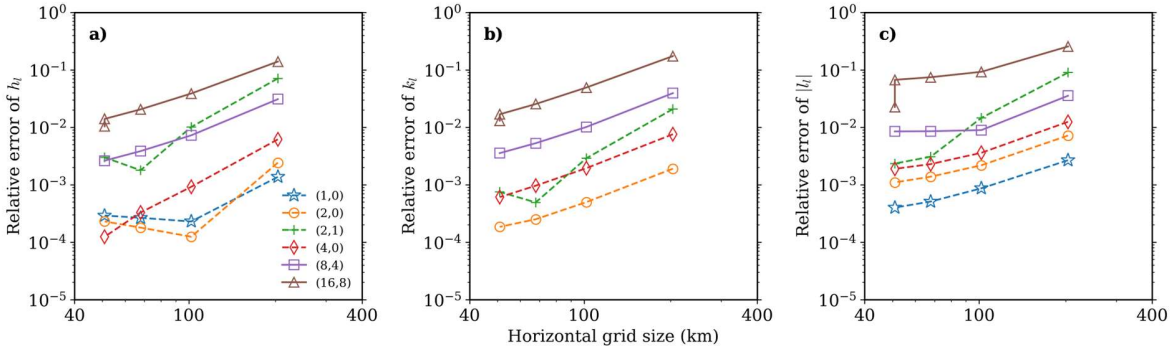

Fig 2. Amplitude errors of Love numbers h (a), k (b) and l (c) as a function of numerical resolutions (i.e., R1-R4, corresponding to horizontal resolutions of approximately 200 to 50 km). For Love number k of loads (1,0), all calculations with different resolutions have a relative error of less than 10^{-5} and are not shown in this figure. Note that R4 and R5 have the same horizontal but different vertical resolutions, and R5 has smaller relative errors compared to R4.

3.2. Glacial isostatic adjustment using ICE-6G_D and VM5a

Since one of the most important applications for CitcomSVE is to model the GIA processes, it is essential to perform a benchmark with glaciation-deglaciation history as surface loads, considering the effects of polar wander, apparent center of mass motion and ocean loads determined by the sea-level equation. A GIA model calculation requires solving governing equations (1)-(3) together with boundary conditions (4)-(5) and the sea-level equation (11) with the floating ice criterion to determine time-dependent gravitational potential anomalies and displacements at the Earth's surface and sea level changes. Note that the same type of benchmark has been published for the incompressible version CitcomSVE-2.1 (Zhong et al., 2022), and we largely follow the setups of that previous work except that the current calculations consider mantle compressibility (i.e., the PREM model), and that the updated sea level equation is used as discussed above and in the supplements (i.e., the AS1 method). As discussed in section 2.3, to deal with the non-linear nature of the sea level equation, multiple (usually 3-4) iterations of complete GIA model runs may be needed (Kendall et al., 2005). CitcomSVE-3.0 fully supports the multiple outer iteration approach using pre- and post-processes to update ocean functions and initial topography. However, in supplementary materials (Supplementary Text 2), we demonstrate how the one-iteration solution method discussed in section 2.3 may be used to achieve adequate accuracy of GIA solutions. In the following GIA benchmark,

455 we compare the results from a single complete CitcomSVE model run with our semi-analytic solutions of
456 the first outer iteration (i.e., the AS1 in the supplementary text), using the pre-calculated ocean functions
457 constructed by assuming the "rigid Earth" and the present-day topography as the initial topography. This
458 comparison ensures that CitcomSVE and semi-analytic calculations have the same ocean functions and
459 initial topography, such that the differences in solutions between CitcomSVE and semi-analytical methods
460 are solely related to numerical errors rather than differences in the models.

461 3.2.1. Definition of the GIA problem.

462 This section presents the setup of the GIA benchmark with ICE-6G_D ice model (Peltier et al.,
463 2015). The Earth model used in this case is the same as the one used for single harmonic loading examples
464 in the previous section. In this case, the surface load consists of a full glaciation-deglaciation cycle, based
465 on the ICE-6G_D ice model (Peltier et al., 2015, 2018) that includes the last 122 thousand years from the
466 last interglacial period to the present day. We assume that Earth was in an equilibrium state at the onset of
467 loading (i.e., 122 ka BP) and that the surface displacements and gravitational potential anomalies since 122
468 ka BP are induced by ice height variations relative to the initial stage and the corresponding change in ocean
469 loads. We computed seven cases using CitcomSVE-3.0 with different spatial-temporal resolutions and cut-
470 off values for the maximum spherical harmonic degrees used in calculating gravitational potential (Table
471 3). Cases GIA_R1, GIA_R2, and GIA_R3 have spatial resolutions of 135 km, 81 km, and 50 km (i.e., a
472 total number of elements of 12x48x48x48, 12x48x80x80, and 12x64x128x128), respectively, and a
473 temporal resolution of 125 years per step. Case GIA_R3_LT is the same as GIA_R3 except with a longer
474 time increment of 250 years per step before LGM (i.e., 26 ka BP). Cases GIA_R3_LT_SH20 and
475 GIA_R3_LT_SH64 have a cut-off value of 20 and 64 for the maximum spherical harmonic degrees,
476 respectively, compared to 32 for other cases. Note that same as CitcomSVE-2.1 (Zhong et al., 2022),
477 computing gravitational potential in the spherical harmonic domain can be computationally expensive. On
478 the other hand, the semi-analytical solution is obtained using spherical harmonic degrees and orders up to
479 256.

It should be noted that in the current implementation, CitcomSVE reads in ice loads defined on regular grids (e.g., 1^{o}x1^{o} grid) and then interpolates the loads to the irregular finite element grids, whereas semi-analytical calculations use spherical harmonic expansions of ice loads to a maximum spherical harmonic degree and order (i.e., 256 in this study) as inputs. The interpolation may cause inconsistent representations of ice loads between CitcomSVE and the semi-analytical calculations. To understand the potential error resulting from the interpolation, we test another case GIA_R3B, which is the same as GIA_R3 except that, for this case, we let CitcomSVE read in ice loads that are computed on CitcomSVE finite element grid points from summing up all the spherical harmonics as used for the analytical solutions, thus avoiding the interpolation from the regular grids to the finite element grids and assuring that CitcomSVE calculations use the exactly same ice loads as that for analytical solutions.

Table 3: Relative Errors for Surface 3-Component Displacement Rates for GIA Benchmark

	GIA_R1	GIA_R2	GIA_R3	GIA_R3B[a]	GIA_R3_LT[b]	GIA_R3_LT_SH20[c]	GIA_R3_LT_SH64
Resolution	48x48x48	48x80x80	64x128x128	64x128x128	64x128x128	64x128x128	64x128x128
Total steps	976	976	976	976	592	592	592
# Cores	96	96	384	384	192	192	384
Runtime (hours)	5.57[d]	4.89	3.01	3.13	3.88	3.34	3.77
Core-hours	535	469	1156	1202	745	641	1448
$\epsilon_r(0)$[e]	17.1% (15.8%)[f]	8.7% (8.1%)	4.9% (4.4%)	4.4% (3.8%)	4.6% (4.4%)	5.0% (4.8%)	4.7% (4.4%)
$\epsilon_{\mathrm{h}}(0)$	14.8% (15.0%)	6.9% (6.9%)	3.9% (3.9%)	3.5% (3.4%)	3.9% (3.9%)	3.9% (3.9%)	3.9% (3.9%)
$\epsilon_g(0)$	10.5% (10.2%)	5.6% (5.6%)	4.7% (4.7%)	4.5% (4.5%)	4.7% (4.7%)	9.2% (9.2%)	3.0% (2.9%)
$\epsilon_r(15)$	7.9% (6.7%)	4.5%(4.1%)	3.4% (3.0%)	2.8% (2.3%)	3.1% (3.0%)	3.1% (3.0%)	3.2% (3.0%)
$\epsilon_h(15)$	4.4% (3.9%)	2.6% (2.4%)	1.8% (1.7%)	1.6% (1.5%)	1.7% (1.7%)	1.7% (1.7%)	1.7% (1.7%)
$\epsilon_g(15)$	14.2% (14.9%)	13.7% (14.3%)	13.6% (14.3%)	13.7% (14.3%)	13.6% (14.3%)	18.3% (19.4%)	7.0% (7.3%)
$\epsilon_r(26)$	7.9% (6.6%)	3.8% (3.3%)	2.8% (2.3%)	2.3% (1.8%)	3.1% (3.0%)	3.0% (2.9%)	3.2% (3.1%)
$\epsilon_h(26)$	4.4% (3.9%)	2.3% (2.0%)	1.5% (1.3%)	1.4% (1.1%)	1.9% (1.8%)	1.9% (1.8%)	1.9% (1.9%)
$\epsilon_g(26)$	6.4% (6.5%)	6.1% (6.2%)	6.1% (6.2%)	6.1% (6.2%)	6.1% (6.2%)	8.2% (8.5%)	3.2% (3.3%)
$\epsilon_{RSL}(15)$[g]	13.1%	2.3%	1.6%	1.3%	1.6%	1.6%	1.6%
$\epsilon_{RSL}(26)$	12.3%	1.8%	1.3%	1.0%	1.3%	1.3%	1.3%

[a] The differences between cases GIA_R3B and GIA_R3 are discussed in section 3.2.1.

[b] The "LT" in GIA_R3_LT represents larger time increments between time steps, where the increments are 250 years and 125 years before and after 26 ka BP, respectively. Cases GIA_R1, GIA_R2, and GIA_R3 have uniform time increment of 125 years.

[c] The "SH20" in GIA_R3_LT_SH20 represents that the cut-off of degrees and orders of spherical harmonics in this calculation is 20. Similarly, case GIA_R3_LT_SH64 has cut off at degrees and orders of 64. Other cases are cut off at degrees and orders of 32.

[d] For this case, the solution converges slowly, causing larger CPU time. All the cases are computed on the NCAR supercomputer Derecho.

[e] ϵ_r, ϵ_h and ϵ_g are errors of displacement rates in radial and horizontal directions and errors of geoid rates, respectively. The errors are given at present-day (0), 15 ka BP, and 26 ka BP. Note that geoid rates include the contribution from the centrifugal potential.

[f] Numbers out of parentheses are errors calculated based on regular grids, whereas numbers inside of parentheses are calculated based on CitcomSVE grids.

[g] ϵ_{RSL} is similar to ϵ_h but for relative sea level. The errors are calculated based on regular grids.

3.2.2. Benchmark results.

We compare the 3-component displacement rates and geoid rates at the surface for three different times (i.e., the present-day, 15 ka BP, and 26 ka BP) obtained from CitcomSVE and the semi-analytical code. Figure 3 shows the present-day displacement rate in vertical, eastern, and northern directions and the present-day geoid rate for case GIA_R3 from CitcomSVE. Large uplift rates at the present day occur in North America, Fennoscandia, and West Antarctica (Fig. 3a), suggesting ongoing rebound induced by ice melting since the last glacial maximum in these regions. Horizontal displacement rates usually have much smaller amplitudes than that in radial direction in those regions.

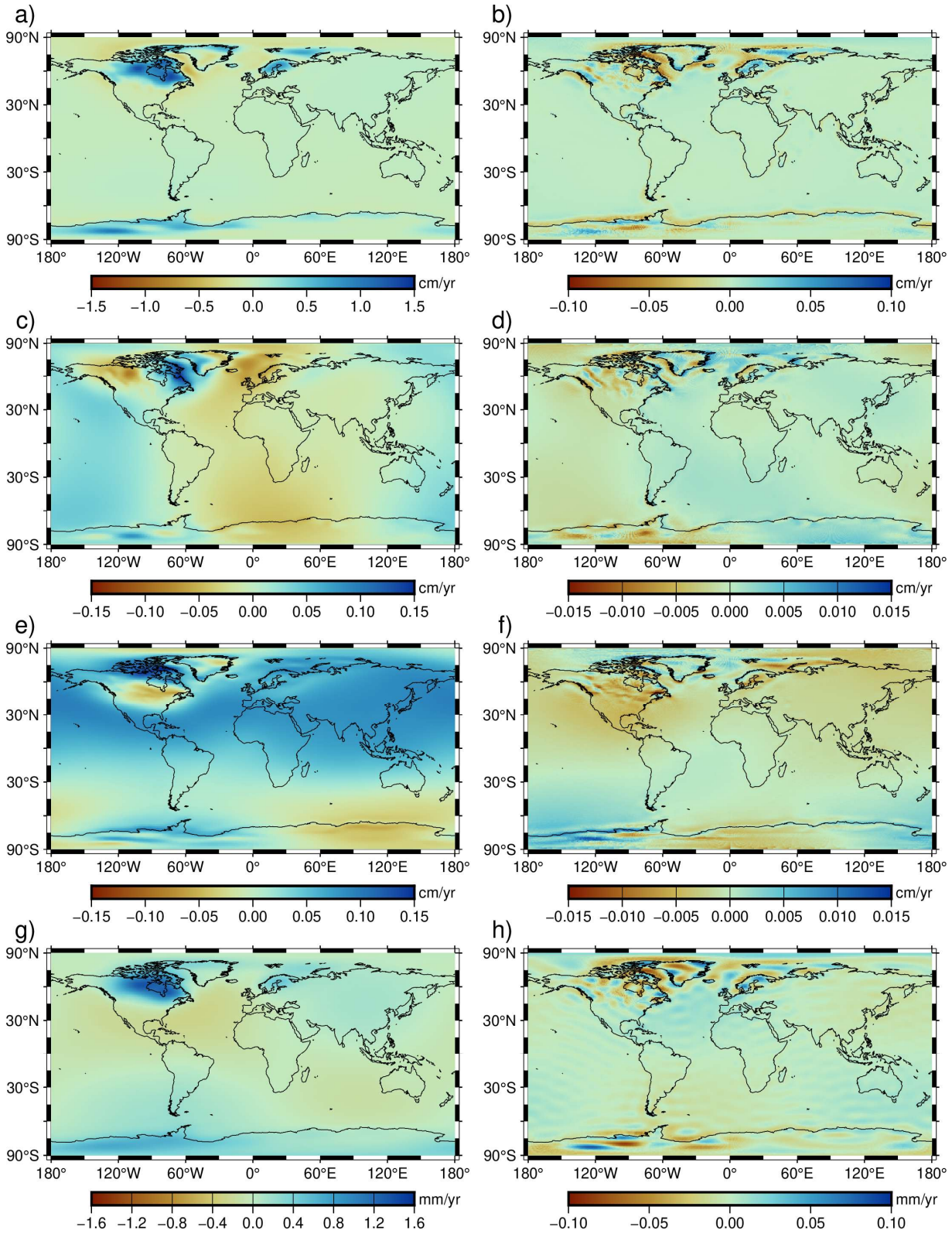

Figure 3. Displacement rate and geoid rate at the present day from case GIA_R3 and their differences to semi-analytical solutions. The top three rows show displacement rates in radial (a), eastern (c), and northern

(e) directions and the differences to semi-analytical solutions for radial (b), eastern (d), and northern (f) directions. The last row shows the geoid rate (g) and its differences to the semi-analytical solution (h).

Figure 3 also shows the differences in present-day displacement rates and geoid rates between CitcomSVE and semi-analytical solutions. The differences are small compared with the magnitudes of displacement rates and geoid rates. Relatively large magnitudes of errors are mainly on short wavelengths (e.g. localized regions), which may partially reflect the fact that CitcomSVE tends to have poorer accuracy at shorter wavelengths (Fig. 1 and 2). Following Zhong et al. (2022), we define relative RMS differences (i.e., errors) in displacement rates between CitcomSVE and semi-analytical solutions as:

$$\varepsilon(t) = \sqrt{\frac{\sum[f_{FE}(\theta,\varphi,t) - f_S(\theta,\varphi,t)]^2}{\sum[f_S(\theta,\varphi,t)]^2}}, \quad (16)$$

where $f_{FE}(\theta,\varphi,t)$ and $f_S(\theta,\varphi,t)$ are the fields of interest at a given time t from CitcomSVE and semi-analytical solutions, respectively, and the summation is based on a regular 1º-by-1º grid. To interpolate the CitcomSVE solutions onto the regular grid, we use the near-neighbor method provided by GMT (Wessel et al., 2019). We also report errors calculated by unweighted summation on the CitcomSVE grid, given the relatively uniform grid size on the spherical surface in CitcomSVE, and the differences in errors from these two ways of calculation are insignificant. We compute errors for radial and horizontal components at three times: present day, 15 ka BP and 26 ka BP. Note that for horizontal error, we square the difference for each horizontal component (i.e., north and east) and add them together for each location.

Table 3 lists the errors for displacement rates, geoid rates, and RSL at these three times for all cases, together with the total CPU time and number of CPUs used for each case. The errors decrease significantly from GIA_R1 to GIA_R3. For Cases GIA_R3, the errors of displacement rates are less than 5%. Case GIA_R3B, which avoids the interpolation of the input ice loads from the regular input grid into CitcomSVE finite element grid to eliminate the potential inconsistency in ice loads between CitcomSVE and semi-analytical calculations, has slightly smaller errors than GIA_R3, indicating a relatively small error induced

by the interpolation. Case GIA_R3_LT with larger time resolution before 26 ka BP has larger errors in displacement rates at 26 ka BP but similar error levels at 15 ka BP and present day. For geoid rates, since CitcomSVE-3.0 only calculates them up to a certain degree (i.e., degree 20, 32, or 64 in our cases), which is much smaller than that used in the analytical solution (i.e., degree 256), the solutions from CitcomSVE-3.0 are lack of short-wavelength features and are much smoother spatially even for cases with high grid resolutions. Therefore, the errors in geoid rates are larger and are generally less sensitive to the model resolutions than to the cut-off degrees. In general, those errors in displacement rates are close to those from CitcomSVE-2.1 (Zhong et al., 2022). CitcomSVE-3.0 is about three times slower than CitcomSVE-2.1 for the same resolutions since internal density variations make the computation more expensive, as discussed in section 2.2. We found that for cases GIA_R1, GIA_R2, and GIA_R3, calculating gravitational potential anomalies takes about one-fourth to half of the total calculation times, depending on the time spent solving the displacement field. It is possible to speed up the calculations of the gravitational potential anomalies by using a grid-based method (e.g., Latychev et al., 2005) or direct integration (e.g., Wang and Li, 2021) for the Poisson equation instead of the currently used spherical harmonic transform. The maximum degree of spherical harmonics used for potential calculation, varying from 20 (GIA_R3_LT_SH20), 32 (GIA_R3_LT) to 64 (GIA_R3_LT_SH64), affects the modeled change rates of geoid and gravity, as shown in the varying errors of geoid rate (Table 3), such that the error reduces with increasing maximum degree. However, it has insignificant effects on surface displacement and RSL (Tables 3 and 4).

We also compare the cumulative radial displacements at different spherical harmonic degrees from CitcomSVE and semi-analytical solutions, following previous works (Paulson et al., 2005; A et al., 2013; Kang et al., 2022; Zhong et al., 2022). The spherical harmonic coefficients of the surface displacement field are provided as an output of CitcomSVE (see Zhong et al., 2022, for the spherical harmonic expansion used in CitcomSVE). The degree amplitude for each l is calculated by

$$a_l(t) = \sqrt{\frac{1}{l+1}\sum_{m=0}^{l}[C_{lm}(t)^2 + S_{lm}(t)^2]}\ , \tag{17}$$

where C_{lm} and S_{lm} denote the cosine and sine parts of the spherical harmonic coefficients expanded from the radial displacement fields at time t. Figures 4a-4c show the amplitude a_l of surface radial displacement at selected spherical harmonics degrees (l=1, 2, 5, 9, 16 and 23) for the three CitcomSVE cases, together with the corresponding semi-analytical solutions. Same as CitcomSVE 2.1 (Zhong et al., 2022), the lowest-resolution case is adequate for relatively long wavelengths (l=1, 2, 5, and 9), whereas higher resolution models are required for accuracy in shorter wavelengths (l=16 and 23) (Fig. 4c). Figure 4d shows the results for the harmonic of l=2 and m=1 that corresponds to the polar wander. Similar to findings from single harmonic benchmarks in the previous section and Zhong et al., (2022), high spatial resolution is required to obtain an accurate solution for the polar wander term. Note that the amplitudes of polar wander mode are much smaller than other long wavelength modes like l=2, 5, and 9.

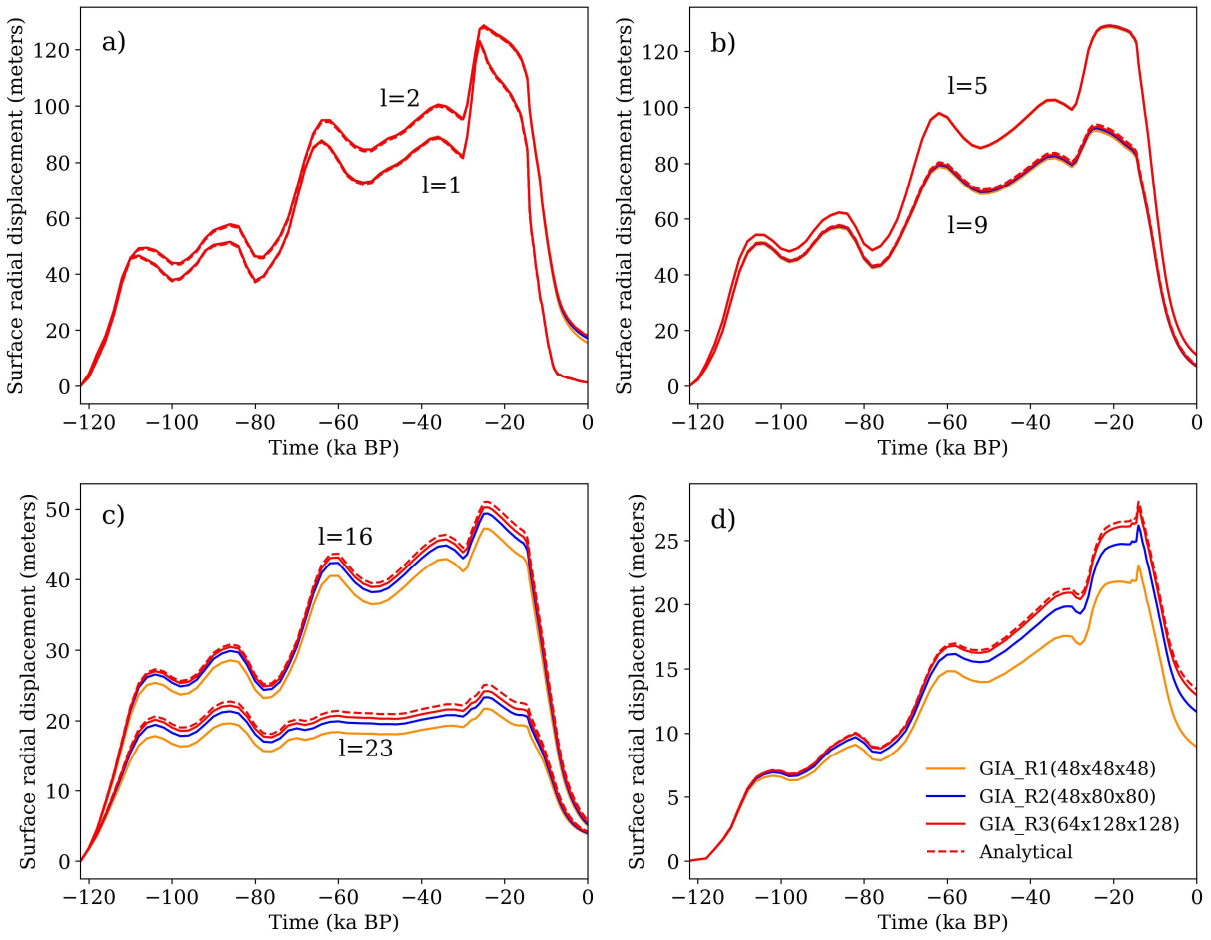

Figure 4. Amplitudes of cumulative radial surface displacement at different spherical harmonic degrees as a function of time for the semi-analytical solutions (Analytical) and three CitcomSVE calculations (GIA_R1, GIA_R2, and GIA_R3) for *l*=1,2 (a), *l*=5,9 (b), *l*=16, 23 (c), and polar wander mode with *l*=2, m=1 (d).

Following Zhong et al., (2022), we use the time-integrated relative error of degree amplitude ε_l to quantify the time-averaged error for a given degree *l*. ε_l is defined as

$$\varepsilon_l = \sqrt{\frac{\int_0^T [a_{l_{FE}}(t) - a_{l_S}(t)]^2 dt}{\int_0^T a_{l_S}(t)^2 dt}}, \quad (18)$$

where $a_{l_{FE}}(t)$ and $a_{l_S}(t)$ represent the degree amplitudes at time t from the CitcomSVE and semi-analytical solutions, respectively, and T is the entire calculation period. The errors for each case are shown in Table 4. As expected, the errors decrease with increasing spatial resolution for each degree, and errors for shorter wavelengths are larger than those for longer wavelengths, except for the polar wander term with relatively large errors.

Table 4 Relative Errors for Surface Radial Displacements at Different Harmonics

	GIA_R1	GIA_R2	GIA_R3	GIA_R3_LT	GIA_R3_LT_SH20	GIA_R3_LT_SH64
ϵ_1	0.97%	0.74%	0.62%	0.64%	0.64%	0.64%
ϵ_2	0.98%	0.76%	0.73%	0.74%	0.74%	0.72%
ϵ_5	0.33%	0.12%	0.13%	0.14%	0.14%	0.14%
ϵ_9	2.30%	1.37%	0.77%	0.77%	0.77%	0.77%
ϵ_{16}	7.56%	3.30%	1.45%	1.45%	1.45%	1.45%
ϵ_{23}	13.66%	6.69%	3.10%	3.10%	N/A[b]	3.10%
$\epsilon_{2,1}$[a]	17.53%	6.58%	1.48%	1.39%	1.39%	1.80%

[a] $\epsilon_{2,1}$ represents the errors for the polar wander term (l=2, m=1).

[b] N/A, the cut-off of degrees and orders of spherical harmonics is 20 for this case, and we only output the spherical harmonics up to the cut-off value in CitcomSVE.

Figure 5 shows the comparisons of modeled relative sea levels at different periods (5 ka BP, 10 ka BP, and 15 ka BP) for GIA_R3 and the semi-analytical solutions on map views. The regions with localized, relatively large errors (Fig. 5b, 5d, and 5f) are mostly around the edges of ice sheets in North America, Fennoscandia, and Antarctica, similar to that for displacement rates, as shown in Figure 3b. Figure 6 compares modeled RSL curves for several sites from semi-analytical solutions and three CitcomSVE calculations with different spatial resolutions. Increasing spatial resolution reduces the offsets to semi-analytical solutions for near-field sites (i.e., sites close to ice sheets) (Fig. 6a and 6b) but does not appear to affect the far-field solutions as much (Fig. 6c and 6d), reflecting that the RSL at far-field sites is not sensitive to numerical resolutions and the offsets to semi-analytical solutions are caused by other factors, for example, the interpolation of ocean function from a regular grid to CitcomSVE grid or the interpolation of results on CitcomSVE grid to RSL sites.

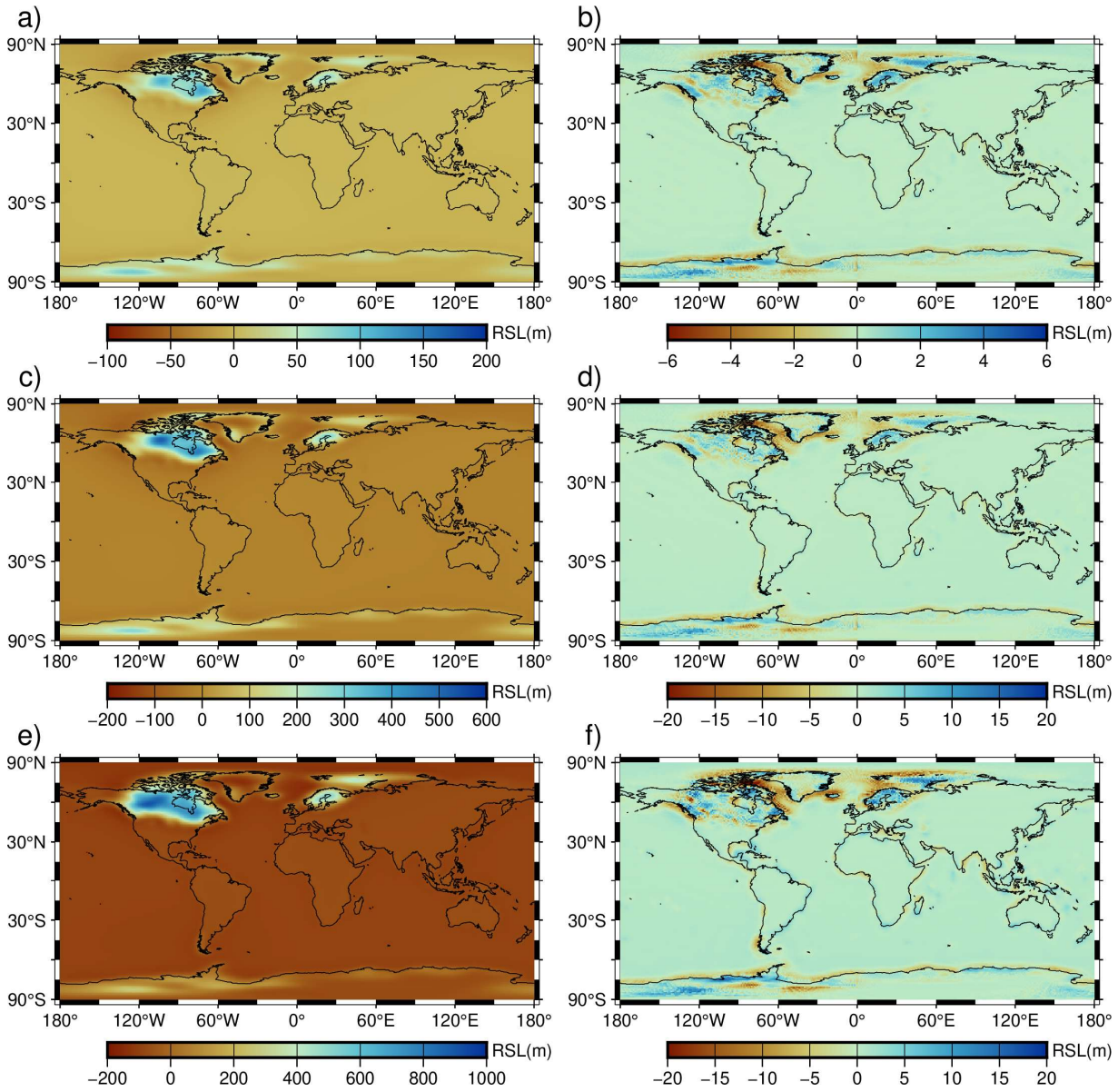

Figure 5. Map of modeled relative sea level at 5 ka BP (a), 10 ka BP (c), and 15 ka BP (e) from GIA_R3 and their differences to semi-analytic solutions at 5 ka BP (b), 10 ka BP (d), and 15 ka BP (f), respectively.

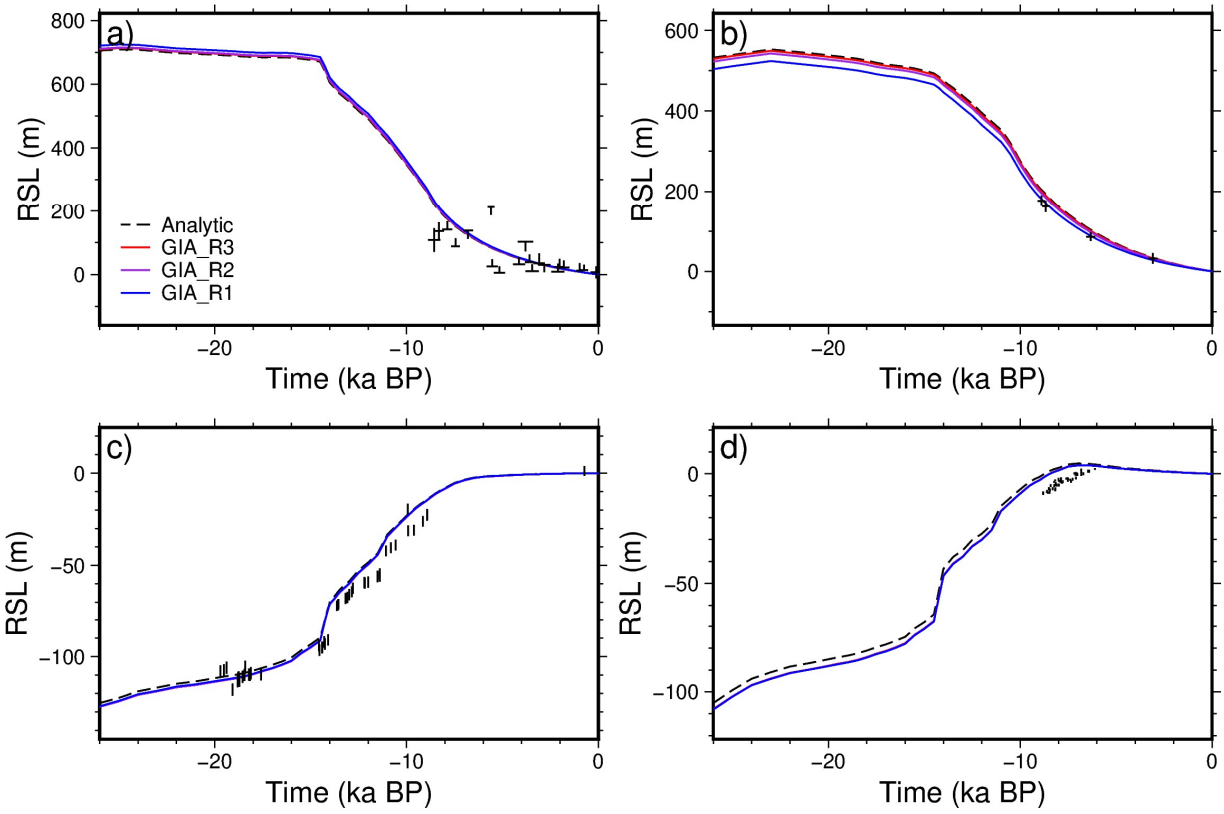

Figure 6. Relative sea-level curves for the last 26 ky at four sites from semi-analytic solutions (Analytic) and three CitcomSVE calculations of different resolutions: cases GIA_R1, GIA_R2, and GIA_R3. The four sites are Churchill (a), Vasterbotten (b), Barbados (c), and Geylang (d) with longitudes and latitudes of (265.60, 58.70), (19.90, 64.00), (300.45, 13.04), and (103.87, 1.31), respectively. The symbols represent the observed RSL changes. The observed RLS are from Peltier et al., (2015) and Lambeck et al., (2014).

4. Conclusion and Discussion

This study introduces CitcomSVE-3.0, an enhanced finite element package that builds upon its predecessor, CitcomSVE-2.1 (Zhong et al., 2022), an efficient package that utilizes massively parallelized computers with up to thousands of CPUs. The new version incorporates elastic compressibility (e.g., the PREM) based on the work of A et al. (2013) and improves the algorithm for solving sea level equations following the work of Kendall et al. (2005), which considers the changes in ocean loads and ocean functions related to ocean-continent transitions and the existence of floating ice. Two benchmark problems are

computed with different numerical resolutions: 1) both surface and tidal loads of different single harmonics and 2) GIA problem with ICE6G_D ice model.

Extensive comparisons between CitcomSVE-3.0 calculations and semi-analytic solutions are presented to validate the accuracy of the CitcomSVE package. The accuracy of CitcomSVE with a horizontal resolution of ~ 50 km is better than 0.1% up to spherical harmonics of degree 4 and better than 2% up to degree 16 in vertical motion and gravitational potential for single harmonic loading problems. The single harmonic benchmarks show that CitcomSVE has a second order of accuracy, i.e., the errors would be reduced to 1/4 if element sizes were reduced by a factor of two. For GIA problems with realistic ice models and dynamically determined ocean loads, the average errors for CitcomSVE models with ~50 km horizontal resolution are less than 5% in displacement rates and relative sea levels.

As shown in the benchmark work for CitcomSVE-2.1 (Zhong et al., 2022), CitcomSVE has a parallel computation efficiency of > 75% for up to 6144 CPU cores. Although CitcomSVE-3.0 is about three times slower than CitcomSVE-2.1 for most of our tests because of the added computational expense for gravitational potential introduced by the layered density structure and compressibility, it can complete a high-resolution global GIA calculation within several hours on supercomputers with a modest number of CPU cores. With its accuracy and efficiency in modeling viscoelastic response to surface loads and tidal forces, the open-source package CitcomSVE has the ability to advance research in planetary and climatic sciences, including GIA-related problems.

Acknowledgement: This work is supported by NSF through grant numbers NSF-EAR 2222115 and NSF-OPP 2333940. Our calculations were performed on parallel supercomputer Derecho operated by the National Center for Atmospheric Research under CISL project codes UCUD0007.

Code and Data Availability Statement: The current version of CitcomSVE3.0 is available from GitHub: https://github.com/shjzhong/CitcomSVE. The exact version of the model used to produce the results used in this paper is archived on Zenodo (10.5281/zenodo.13932410), as are input data (including the ice model and Earth model used in this paper) and scripts to run the model and produce the plots for all the calculations presented in this paper.

Author contribution: All authors contributed to the development of the code, design of the research, analysis of the results, and writing of the manuscript. T.Y. performed numerical calculations.

Competing interests: The authors declare no competing interests in this work.

Reference

A, G., Wahr, J., and Zhong, S.: Computations of the viscoelastic response of a 3-D compressible Earth to surface loading: an application to Glacial Isostatic Adjustment in Antarctica and Canada, Geophysical Journal International, 192, 557–572, https://doi.org/10.1093/gji/ggs030, 2013.

Bagge, M., Klemann, V., Steinberger, B., Latinović, M., and Thomas, M.: Glacial-Isostatic Adjustment Models Using Geodynamically Constrained 3D Earth Structures, Geochemistry, Geophysics, Geosystems, 22, e2021GC009853, https://doi.org/10.1029/2021GC009853, 2021.

Bevis, M., Wahr, J., Khan, S. A., Madsen, F. B., Brown, A., Willis, M., Kendrick, E., Knudsen, P., Box, J. E., van Dam, T., Caccamise, D. J., Johns, B., Nylen, T., Abbott, R., White, S., Miner, J., Forsberg, R., Zhou, H., Wang, J., Wilson, T., Bromwich, D., and Francis, O.: Bedrock displacements in Greenland manifest ice mass variations, climate cycles and climate change, Proceedings of the National Academy of Sciences, 109, 11944–11948, https://doi.org/10.1073/pnas.1204664109, 2012.

Farrell, W. E. and Clark, J. A.: On Postglacial Sea Level, Geophysical Journal International, 46, 647–667, https://doi.org/10.1111/j.1365-246X.1976.tb01252.x, 1976.

Fienga, A., Zhong, S., Mémin, A., and Briaud, A.: Tidal dissipation with 3-D finite element deformation code CitcomSVE v2.1: comparisons with the semi-analytical approach, in the context of the Lunar tidal deformations, Celest Mech Dyn Astron, 136, 43, https://doi.org/10.1007/s10569-024-10202-6, 2024.

French, S. W. and Romanowicz, B.: Broad plumes rooted at the base of the Earth's mantle beneath major hotspots, Nature, 525, 95–99, https://doi.org/10.1038/nature14876, 2015.

Gomez, N., Latychev, K., and Pollard, D.: A Coupled Ice Sheet–Sea Level Model Incorporating 3D Earth Structure: Variations in Antarctica during the Last Deglacial Retreat, Journal of Climate, 31, 4041–4054, https://doi.org/10.1175/JCLI-D-17-0352.1, 2018.

Han, D. and Wahr, J.: The viscoelastic relaxation of a realistically stratified earth, and a further analysis of postglacial rebound, Geophysical Journal International, 120, 287–311, https://doi.org/10.1111/j.1365-246X.1995.tb01819.x, 1995.

Huang, P., Steffen, R., Steffen, H., Klemann, V., Wu, P., van der Wal, W., Martinec, Z., and Tanaka, Y.: A commercial finite element approach to modelling Glacial Isostatic Adjustment on spherical self-gravitating compressible earth models, Geophysical Journal International, 235, 2231–2256, https://doi.org/10.1093/gji/ggad354, 2023.

Ivins, E. R., van der Wal, W., Wiens, D. A., Lloyd, A. J., and Caron, L.: Antarctic upper mantle rheology, Geological Society, London, Memoirs, 56, 267–294, https://doi.org/10.1144/M56-2020-19, 2023.

Kang, K., Zhong, S., Geruo, A., and Mao, W.: The effects of non-Newtonian rheology in the upper mantle on relative sea level change and geodetic observables induced by glacial isostatic adjustment process, GEOPHYSICAL JOURNAL INTERNATIONAL, 228, 1887–1906, https://doi.org/10.1093/gji/ggab428, 2022.

695 Kendall, R. A., Mitrovica, J. X., and Milne, G. A.: On post-glacial sea level - II. Numerical formulation and
696 comparative results on spherically symmetric models, Geophysical Journal International, 161, 679–706,
697 https://doi.org/10.1111/j.1365-246X.2005.02553.x, 2005.

698 Klemann, V., Martinec, Z., and Ivins, E. R.: Glacial isostasy and plate motion, Journal of Geodynamics, 46,
699 95–103, https://doi.org/10.1016/j.jog.2008.04.005, 2008.

700 Lambeck, K., Rouby, H., Purcell, A., Sun, Y., and Sambridge, M.: Sea level and global ice volumes from the
701 Last Glacial Maximum to the Holocene, Proceedings of the National Academy of Sciences, 111, 15296–
702 15303, https://doi.org/10.1073/pnas.1411762111, 2014.

703 Lambeck, K., Purcell, A., and Zhao, S.: The North American Late Wisconsin ice sheet and mantle viscosity
704 from glacial rebound analyses, Quaternary Science Reviews, 158, 172–210,
705 https://doi.org/10.1016/j.quascirev.2016.11.033, 2017.

706 Latychev, K., Mitrovica, J. X., Tromp, J., Tamisiea, M. E., Komatitsch, D., and Christara, C. C.: Glacial isostatic
707 adjustment on 3-D Earth models: a finite-volume formulation, Geophysical Journal International, 161,
708 421–444, https://doi.org/10.1111/j.1365-246X.2005.02536.x, 2005.

709 Lloyd, A. J., Wiens, D. A., Zhu, H., Tromp, J., Nyblade, A. A., Aster, R. C., Hansen, S. E., Dalziel, I. W. D.,
710 Wilson, T. j., Ivins, E. R., and O'Donnell, J. P.: Seismic Structure of the Antarctic Upper Mantle Imaged with
711 Adjoint Tomography, Journal of Geophysical Research: Solid Earth, 125,
712 https://doi.org/10.1029/2019JB017823, 2020.

713 Longman, I. M.: A Green's function for determining the deformation of the Earth under surface mass
714 loads: 2. Computations and numerical results, Journal of Geophysical Research (1896-1977), 68, 485–496,
715 https://doi.org/10.1029/JZ068i002p00485, 1963.

716 Martinec, Z.: Spectral-finite element approach to three-dimensional viscoelastic relaxation in a spherical
717 earth, Geophys. J. Int., 142, 117–141, https://doi.org/10.1046/j.1365-246x.2000.00138.x, 2000.

718 Milne, G. A., Davis, J. L., Mitrovica, J. X., Scherneck, H.-G., Johansson, J. M., Vermeer, M., and Koivula, H.:
719 Space-Geodetic Constraints on Glacial Isostatic Adjustment in Fennoscandia, Science, 291, 2381–2385,
720 https://doi.org/10.1126/science.1057022, 2001.

721 Mitrovica, J., Tamisiea, M., Davis, J., and Milne, G.: Recent mass balance of polar ice sheets inferred from
722 patterns of global sea-level change, NATURE, 409, 1026–1029, https://doi.org/10.1038/35059054, 2001.

723 Mitrovica, J. X., Davis, J. L., and Shapiro, I. I.: A spectral formalism for computing three-dimensional
724 deformations due to surface loads: 2. Present-day glacial isostatic adjustment, Journal of Geophysical
725 Research: Solid Earth, 99, 7075–7101, https://doi.org/10.1029/93JB03401, 1994.

726 Paulson, A., Zhong, S., and Wahr, J.: Modelling post-glacial rebound with lateral viscosity variations,
727 Geophysical Journal International, 163, 357–371, https://doi.org/10.1111/j.1365-246X.2005.02645.x,
728 2005.

729 Peltier, W. R.: Postglacial variations in the level of the sea: Implications for climate dynamics and solid-
730 Earth geophysics, Reviews of Geophysics, 36, 603–689, https://doi.org/10.1029/98RG02638, 1998.

731 Peltier, W. R., Argus, D. F., and Drummond, R.: Space geodesy constrains ice age terminal deglaciation:
732 The global ICE-6G_C (VM5a) model: Global Glacial Isostatic Adjustment, J. Geophys. Res. Solid Earth, 120,
733 450–487, https://doi.org/10.1002/2014JB011176, 2015.

734 Peltier, W. R., Argus, D. F., and Drummond, R.: Comment on "An Assessment of the ICE-6G_C (VM5a)
735 Glacial Isostatic Adjustment Model" by Purcell et al., Journal of Geophysical Research: Solid Earth, 123,
736 2019–2028, https://doi.org/10.1002/2016JB013844, 2018.

737 Qin, C., Zhong, S., and Wahr, J.: A perturbation method and its application: elastic tidal response of a
738 laterally heterogeneous planet, Geophysical Journal International, 199, 631–647,
739 https://doi.org/10.1093/gji/ggu279, 2014.

740 Ritsema, J., Deuss, A., van Heijst, H. J., and Woodhouse, J. H.: S40RTS: a degree-40 shear-velocity model
741 for the mantle from new Rayleigh wave dispersion, teleseismic traveltime and normal-mode splitting
742 function measurements, Geophysical Journal International, 184, 1223–1236,
743 https://doi.org/10.1111/j.1365-246X.2010.04884.x, 2011.

744 Takeuchi, H.: On the Earth tide of the compressible Earth of variable density and elasticity, Eos,
745 Transactions American Geophysical Union, 31, 651–689, https://doi.org/10.1029/TR031i005p00651,
746 1950.

747 Tanaka, Y., Klemann, V., Martinec, Z., and Riva, R. E. M.: Spectral-finite element approach to viscoelastic
748 relaxation in a spherical compressible Earth: application to GIA modelling: Postglacial rebounds in a
749 compressional Earth, Geophysical Journal International, 184, 220–234, https://doi.org/10.1111/j.1365-
750 246X.2010.04854.x, 2011.

751 Tromp, J.: Seismic wavefield imaging of Earth's interior across scales, Nat Rev Earth Environ, 1, 40–53,
752 https://doi.org/10.1038/s43017-019-0003-8, 2020.

753 Wang, Y. and Li, M.: The interaction between mantle plumes and lithosphere and its surface expressions:
754 3-D numerical modelling, Geophysical Journal International, 225, 906–925,
755 https://doi.org/10.1093/gji/ggab014, 2021.

756 Weerdesteijn, M. F. M., Naliboff, J. B., Conrad, C. P., Reusen, J. M., Steffen, R., Heister, T., and Zhang, J.:
757 Modeling Viscoelastic Solid Earth Deformation Due To Ice Age and Contemporary Glacial Mass Changes in
758 ASPECT, Geochem Geophys Geosyst, 24, https://doi.org/10.1029/2022GC010813, 2023.

759 Wessel, P., Luis, J. F., Uieda, L., Scharroo, R., Wobbe, F., Smith, W. H. F., and Tian, D.: The Generic Mapping
760 Tools Version 6, Geochemistry, Geophysics, Geosystems, 20, 5556–5564,
761 https://doi.org/10.1029/2019GC008515, 2019.

762 Wu, P.: Using commercial finite element packages for the study of earth deformations, sea levels and the
763 state of stress, Geophysical Journal International, 158, 401–408, https://doi.org/10.1111/j.1365-
764 246X.2004.02338.x, 2004.

765 Wu, P. and Peltier, W. R.: Viscous gravitational relaxation, Geophysical Journal International, 70, 435–485,
766 https://doi.org/10.1111/j.1365-246X.1982.tb04976.x, 1982.

Yuan, T.: Dataset for CitcomSVE 3.0: A Three-dimensional Finite Element Software Package for Modeling Load-induced Deformation for an Earth with Viscoelastic and Compressible Mantle, https://doi.org/10.5281/zenodo.13932411, 2024.

Zhong, S., Zuber, M. T., Moresi, L., and Gurnis, M.: Role of temperature-dependent viscosity and surface plates in spherical shell models of mantle convection, Journal of Geophysical Research: Solid Earth, 105, 11063–11082, https://doi.org/10.1029/2000JB900003, 2000.

Zhong, S., Paulson, A., and Wahr, J.: Three-dimensional finite-element modelling of Earth's viscoelastic deformation: effects of lateral variations in lithospheric thickness, Geophysical Journal International, 155, 679–695, https://doi.org/10.1046/j.1365-246X.2003.02084.x, 2003.

Zhong, S., Zhang, N., Li, Z., and Roberts, J.: Supercontinent cycles, true polar wander, and very long-wavelength mantle convection, EARTH AND PLANETARY SCIENCE LETTERS, 261, 551–564, https://doi.org/10.1016/j.epsl.2007.07.049, 2007.

Zhong, S., McNamara, A., Tan, E., Moresi, L., and Gurnis, M.: A benchmark study on mantle convection in a 3-D spherical shell using CitcomS, Geochemistry, Geophysics, Geosystems, 9, https://doi.org/10.1029/2008GC002048, 2008.

Zhong, S., Qin, C., Geruo, A., and Wahr, J.: Can tidal tomography be used to unravel the long-wavelength structure of the lunar interior?, GEOPHYSICAL RESEARCH LETTERS, 39, https://doi.org/10.1029/2012GL052362, 2012.

Zhong, S., Kang, K., A, G., and Qin, C.: CitcomSVE: A Three-Dimensional Finite Element Software Package for Modeling Planetary Mantle's Viscoelastic Deformation in Response to Surface and Tidal Loads, Geochem Geophys Geosyst, 23, https://doi.org/10.1029/2022GC010359, 2022.